The Metrewavelength Sky
ASI Conference Series, 2014, Vol. 13, pp 333 – 338
Edited by J. N. Chengalur & Y. Gupta

High sensitivity wide-band wide-field at low radio frequencies

S. Bhatnagar* and U. Rau
National Radio Astronomy Observatory, Socorro, NM-87801, USA

Abstract. High sensitivity imaging at low radio frequencies require wide-band receivers and long baselines. This, in combination with inherently stronger and more complex sky brightness, translates to a requirement of high dynamic range imaging using vast quantities of data. Additionally, wide field of view also requires accounting for many time- and frequency-dependent instrumental effects to achieve thermal noise limited images. These effects are in general also directionally dependent (DD) and require use of advanced imaging algorithms which are inherently also more compute intensive.

This paper gives an overview of the status of the projection algorithms to correct for the DD effects due to the antenna primary beam (BP) and demonstrate the improvements in imaging performance afforded by these new algorithms. Larger data volume and need for more compute-expensive imaging algorithms couples algorithm design and High Performance Computing (HPC) techniques. This is a major challenge, particularly in low frequency imaging. We briefly mention some of the HPC solutions being currently pursued in the community.

Keywords : radio interferometry – imaging – low radio frequency

1. Introduction

Two issues that impact the imaging challenges at low radio frequencies and the achievable RMS noise are: (a) nature of the sky brightness at low frequencies, and (b) sky confusion noise limit. Figure 1 shows an image from a simulation of the expected sky brightness distribution[1] at 1.4 GHz. At a flux limit of 1 μJy, the sky is crowded

*email: sbhatnag@nrao.edu

[1]This simulation excludes e extended emission, which become important at resolution of about $\geq 2''$.

and sources detected out to at least the first primary beam (PB) side lobe. Assuming the highest sidelobe of the telescope point spread function (PSF) at the 1% level, to reach a 1μJy/beam RMS noise would require deconvolving all sources >100μJy. The number of sources greater than 100 μJy per square degree at frequencies below 300 MHz are in the 10^{2-3} range and the total integrated flux in the several Jy range with a few 1 Jy-sources per square degree. The implications for the imaging problem is that wide-field, high dynamic range (ratio of peak brightness to the RMS noise) imaging involving deconvolution of crowded fields is an inevitable consequence of high sensitivity imaging at low frequencies.

The sky background confusion noise is proportional to $\nu^{-2.7}/B_{max}$, where B_{max} is the maximum baseline length. Thermal-noise limited imaging therefore requires sufficiently long baselines to reduce the sky confusion noise to a level below the thermal noise limit of the telescope. The right panel of figure 1 shows the plot of the estimated sky background confusion noise at 1400, 200 and 100 MHz as a function of the baseline length. The plots shows that observations with a thermal noise limit of 1μJy/beam at 1400, 200 and 100 MHz require maximum baseline length of approximately 10, 100 and 300 Km respectively. High sensitivity imaging at low frequencies therefore necessarily requires wide-band receivers, long baselines and wide-field high dynamic range imaging capability. Wide-field imaging in-turn requires imaging algorithms that also correct for various direction-dependent (DD) effects. We will come back to this point in section 2.

1.1 Data volume

Computing and data I/O load for imaging is directly proportional to the data volume, which in-turn increases with baseline length and bandwidth. The total data volume collected from an aperture synthesis telescope with N_a antennas, N_c frequency channels, N_T time snapshot and N_p polarization products is given by

$$Data\ Volume = \frac{N_a(N_a-1)}{2} \times N_c \times N_T \times N_p \times (Bytes\ Per\ Sample) \qquad (1)$$

Taking into account the bandwidth and time smearing limits (Thompson et al. 2001), N_c and N_T is given by

$$N_c = \frac{N_{PBS\,idelobes} B_{max}}{\eta D} \frac{\Delta\nu}{\nu_\circ} \qquad N_T = \frac{N_{PBS\,idelobes} B_{max}}{\eta D} \omega_e T \qquad (2)$$

where $N_{PBS\,idelobes}$ is the number of antenna primary beam (PB) sidelobes (a measure of the FoV; $N_{PBS\,idelobes} = 1$ for the PB main lobe), $\Delta\nu$ is the total bandwidth, T is the total integration time, η is the tolerance for the fractional loss in amplitude due to smearing, D is the diameter of the antenna elements and ω_e is the earth angular rotation speed in $rad\ sec^{-1}$.

The thermal noise limit of an interferometric telescope is inversely proportional

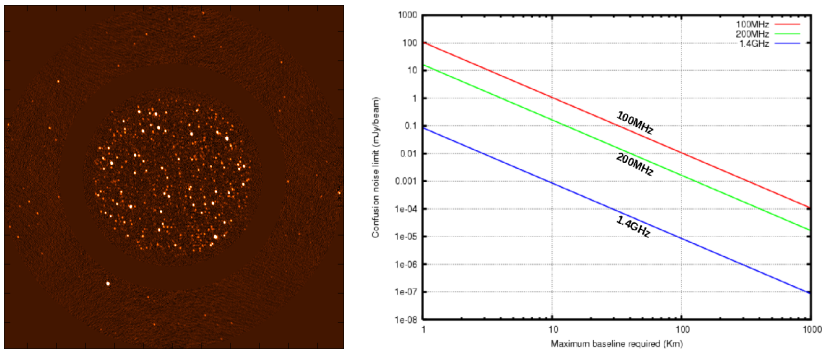

Figure 1. The imaging the left panel shows a simulation of the sky brightness distribution at 1.5 GHz with a lower flux limit of 1 μJy. The plot in the right plane shows the estimated sky background confusion noise as a function of baseline length at 100, 200 and 1400 MHz.

to $N_a \sqrt{T\ \Delta\nu}$. To take an example, an 8^h observations with a fractional bandwidth of $\sim 67\%$ requires $N_c \sim 10^3$, $N_T \sim\ few \times 10^3$ and $N_{PBS idelobes} \geq 2$. Using 30 bytes per sample and $\eta = 0.05$, a telescope with $N_a = 30$ and $B_{max} = 30$ Km generates a few Tera bytes of data. Data volume at 100 MHz will be about 10 times larger. Data from future telescopes like the SKA is estimated to be 10^{3-6} times larger.

High sensitivity imaging at low frequencies therefore requires wide-band receivers, long baselines and use of wide-field imaging algorithms to image large data volume. In the sections below, we give an overview of the projection algorithms to correct for the effects of the antenna primary beam and wide-band modeling of the sky brightness distribution for wide-band wide-field imaging (but also see Nijboer & Noordam (2007); Mitchell et al. (2008)) and show the results from imaging of wide-band data in the 1 – 2 GHz band. We also briefly mention the resulting high performance computing (HPC) problem and the various solutions being pursued in the community.

2. Wide-band wide-field effects

The measurement equation to describe a measurement from a single interferometer with baseline vector $\vec{b}_{ij}$ and calibrated for the direction independent (DI) effects is given by

$$V_{ij}(\nu) = W_{ij} \iint P_{ij}(\vec{s}, \nu, t)\ I(\vec{s}, \nu)\ e^{\iota \vec{s} \cdot \vec{b}_{ij}}\ d\vec{s} \tag{3}$$

where $\vec{s}$ is the direction in the sky, W_{ij} is the measurement weight for the baseline $i - j$, P_{ij} is the combined sensitivity pattern of the antenna i and j and I is the sky brightness distribution. The dominant direction dependent (DD) effects in wide-field wide-band imaging come from antenna PB (P_{ij}). With a 2:1 bandwidth ratio of typical modern wide-band receivers, the PB also changes across the frequency band (e.g., by a factor of 2 in width). The PB is typically also rotationally asymmetric. As

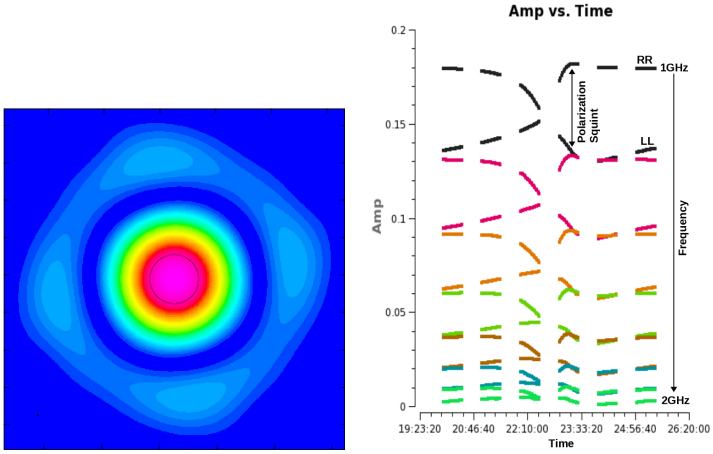

Figure 2. The image on the left shows a model for the EVLA primary beam at 1.4 GHz. The rotation with time, scaling with frequency and polarization squint together lead the variations in the observed amplitude of a compact source at the 50% point of the PB at reference frequency, shown in the plot on the right. Each set of the "X" shaped curves correspond to the amplitude at a particular frequency. The two curves in each set correspond to the amplitude of the RR and LL parallel-hand polarization products as a function of time.

an example, Fig. 2 shows a model of the EVLA PB at 1.4 GHz. The antenna PB, projected on the sky, rotates with the parallactic angle. Wide-band observations with El-Az mount antennas therefore suffer from time- and frequency-varying DD effects which, if ignored, limit the imaging performance to significantly higher than telescope thermal noise limit. The plot in the right-hand panel of Fig. 2 shows the variations in the observed amplitude (from a source located at the half-power point of the PB at the reference frequency) as a function of time, frequency and polarization for a compact unpolarized source. Power in the two parallel hand polarization products (labeled as RR and LL) is different and varies with time due to the combination of rotation of the PB with PA and the polarization squint in the EVLA antenna optics. The variation in the RR- and LL-amplitude as a function of frequency is due to the frequency dependence of the PB. The effects in the image domain when all these PB effects are ignored during imaging are shown in the top-left image in Fig. 3. The "noise" in the image is dominated by the artifacts due to the DD effects of the PB.

3. The WB A-projection algorithm

Equation 3 can be written entirely in the data (visibility) domain as

$$V_{ij}(\nu) = A_{ij}(\nu, t) \star V^{\circ}_{ij}(\nu, t) \tag{4}$$

where A_{ij} is the convolution of the two antenna aperture illumination patterns, V°_{ij} is the Fourier transform of the true sky brightness distribution as measured at baseline

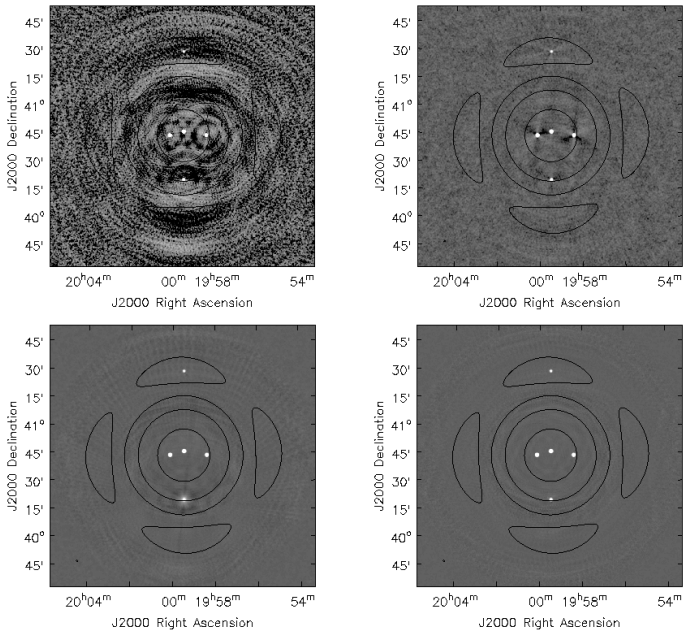

Figure 3. Top-left: Standard imaging ignoring PB effects and frequency dependence of the sky brightness. Top-right: Standard imaging with MS-MFS algorithm to account for frequency dependence of the sky brightness. Bottom-left: Combination of the MS-MFS algorithm and narrow-band A-Projection algorithm which ignores the frequency dependence of the PB. Bottom-right: Combined WB A-Projection and MS-MFS algorithm were all PB effects as well as the frequency dependence of the sky brightness is taken into account.

$i-j$ and "$\star$" represents the convolution operator. A_{ij} represents the antenna PB in the data domain and includes all the time, frequency and polarization dependent effects shown in Fig. 2. Since the image corresponds to an integral over time, frequency and polarization, these PB effects need to be projected-out *prior* to (or as part of) the transformation to the image domain. The WB A-Projection (Bhatnagar et al. 2013) projects-out the PB effects by constructing a function X_{ij} (called the conjugate operator) with has the property that $X_{ij} \star A_{ij}$ becomes nearly independent of time, frequency and polarization. The imaging algorithm then uses X_{ij} as part of the transform to convert the data to the image domain. With an appropriate image-domain normalization, the PB effects mentioned above are projected out and the resulting image is free of its limiting effects (see Bhatnagar et al. (2013) for details). The image in the bottom right panel of Fig. 2 shows the image formed using the combined WB A-Projection algorithm to account for the PB effects along with the Multi-scale MFS (MS-MFS) algorithm (Rau & Cornwell 2011) to also simultaneously account for the frequency dependence of the sky brightness distribution (the sources in these images have a spectral index of 0.5). The artifacts due to the PB effects and the frequency dependence of the sky brightness are clearly removed. Results from intermediate algorithms where

the time dependence of the PB is ignored and the frequency dependence of the PB is absorbed in the frequency dependence of the sky brightness are shown in the images in the top-right and bottom-left panels. The residual artifacts in these images are also significant, implying that the combined algorithm to *simultaneously* project-out PB effects and account for frequency dependence of the sky brightness is required for thermal-noise limited imaging.

4. Computing load

The WB A-Projection and the MS-MFS algorithms both require more computing than the conventional imaging algorithms. The computing load of the WB A-Projection algorithm linearly increase with the data volume and the bandwidth. The computing cost of MT-MFS depends on the image size and the complexity of the sky brightness distribution. With several orders of magnitude larger data volumes and larger FoV (requiring larger images), imaging at low frequencies requires deploying the imaging algorithms on HPC platforms to mitigate the run-time data I/O and computational costs. In the various HPC solutions being currently pursued in the community, run-time costs are mitigated by serving the data from parallel file system like the `Lustre` file system connected to a cluster of computers for parallel computing (Bhatnagar et al. 2009). The dominant cost in imaging comes from the need to re-sample the raw data on a regular grid. Computing solutions using massively parallel systems like GP-GPUs (Romein 2012; Muscat 2013) are being pursued to mitigate the run-time cost of this operation. These solutions are expected to solve the computing problem with existing low-frequency telescopes. However with several order of magnitude higher data rates and image sizes required for future telescopes like the SKA, a different post-processing paradigm, possibly involving streaming processing will be necessary.

Acknowledgements

Work related to the some of the work reported here was done in collaboration with K. Golap and T. J. Cornwell over the years.

References

Bhatnagar S., Rau U., Golap K., 2013, ApJ, 770, 91

Bhatnagar S., Ye H., Schiebel D., 2009, Parallelization of the off-line data processing using CASA, Technical report, EVLA Memo 133

Mitchell D. A., Greenhill L. J., Wayth R. B., Sault R. J., Lonsdale C. J., Cappallo R. J., Morales M. F., Ord S. M., 2008, IEEE Journal of Selected Topics in Signal Processing, issue 5 2, 707

Muscat D., 2013, Master's thesis, University of Malta, Malta

Nijboer R. J., Noordam J. E., 2007, ASP Conf. Series: ADASS XVII 376, 237

Rau U., Cornwell T. J., 2011, A&A, 532, A71

Romein J. W., 2012, in ICS'12 International Con, 321

Thompson A. R., Moran J. M., Swenson, Jr. G. W., 2001, Interferometry and Synthesis in Radio Astronomy (2^{nd} edition), John Wiley